Forest fires smoke monitoring
from Sea-viewing Wide Field-of-view Sensor images

Abdellatif HASSINI[1,*], Sébastien DÉJEAN[2], Noureddine BENABADJI[1],
Noureddine HASSINI[3], Ahmed Hafid BELBACHIR[1]

[1]Laboratory of Application and Analysis of Radiations LAAR,
 Department of Physics USTOMB. El M'nouer B.P.1505 Oran, Algeria

[2]Institute of Mathematics of Toulouse, UMR CNRS 5219,
 University Paul Sabatier, 31062, Toulouse cedex 9, France

[3]Department of Biology, University of Oran Es-senia, Oran, Algeria

*Corresponding author: abdelatif_hassini@yahoo.com

A method for detecting forest fires smoke using *SeaWiFS* (Sea-viewing Wide Field-of View Sensor) images is developed in this paper. The colour masking technique is proposed to extract the maximum fires smoke pixels from the *SeaStar*/*SeaWiFS* satellite images by using Fusion by Arithmetic Combination (*FAC*) of the spectral bands method. Each image used is converted from RGB (Red, Green, Blue) to HIS (Hue, Saturation, Intensity) system. The resulting smoke plumes pixels are obtained visually in the Intensity and Saturation images. Then the values of intensity and saturation are analyzed to be potentially applied in other images. In this research, we applied our detecting forest fires smoke algorithm in seven different scenes, and in a variety of conditions, including different regions of the planet, and different dates. Next, Smoke Pixel Reference Ratio (*SPRR*) was used to test the proposed method. We found that the method can detect maximum pixels of smoke plumes in spite of some limitations.

Keywords: remote sensing, forest fires, image processing, smoke.

1. Introduction

Biomass burning has tremendous impact on the Earth's ecosystems and climate, for it drastically alters the landscape and vegetation patterns and emits large amounts of greenhouse gases and aerosol particles [1–3]. Smoke aerosols may interact with cloud droplets [4, 5] and alter considerably the Earth's radiation budget [6, 7]. Assessment and understanding of the wide-reaching and long-lasting effects of fires on the envi-

ronment and climate entails a good knowledge of the spatial distribution and temporal variation of fire activity on a global scale [8]. This may be achieved only through the use of remote sensing technologies, which provide an efficient and economical means of acquiring fire information over large areas on a routine basis, despite various limitations and shortcomings [9, 10].

A forest fire can be a real ecological disaster, regardless of whether it is caused by natural forces or human activity. It is impossible to control nature, but it is possible to map forest fire risk zones and thereby minimise the frequency of fire, avert damage, *etc.* [11].

Automated fire detection algorithms are used for NOAA's Geostationary Operational Environmental Satellites (GOES-10 and 12) and Polar Orbiting Operational Environmental Satellites (POES, NOAA-15, 16 and 17). The Moderate Resolution Imaging Spectroradiometer (MODIS) from NASA's Terra and Aqua spacecraft (MODIS fire detection) is performed using a contextual algorithm that exploits the strong emission of mid-infrared radiation from fires. The algorithm examines each pixel of the MODIS swath and ultimately assigns to each one of the following classes: missing data, cloud, water, non-fire, fire, or unknown. The Wildfire Automated Biomass Burning Algorithm (WF_ABBA) is employed for GOES imagery. The WF_ABBA is a dynamic multi-spectral thresholding contextual algorithm that uses the visible (when available), 3.9 µm, and 10.7 µm, infrared bands to locate and characterize hot spot pixels. Descriptions of the algorithm can be found at the link: http://cimss.ssec.wisc.edu/goes/burn/publications.html.

The NOAA polar orbiting satellites use the Fire Identification Mapping and Monitoring Algorithm (FIMMA), which is described at link: http://www.ssd.noaa.gov/PS/FIRE/Layers/FIMMA/fimma.html.

Fire detects from MODIS are obtained using the algorithms described at http://modis-fire.gsfc.nasa.gov/methodology.asp.

It should be noted that many of the fires detected by these algorithms are not wildfires but rather agricultural or control burns and there is no attempt to distinguish between the two [12]. The most serious problems suffered by NOAA algorithms are caused by the saturation of channel 3 (3.7 µm) in AVHRR (Advanced Very High Resolution Radiometer) and its contamination by solar reflection. The problem is anticipated to be resolved or lessened by the MODIS sensors due to the inclusion of a special fire channel (3.9 µm instead of 3.7 µm) that has a wider dynamic range and is less influenced by solar reflection [13]. The most challenging is to account for the contribution of solar radiation due to the reflection from cloud and Earth's surfaces. The majority of the algorithms include cloud screening tests that are reasonably efficient in removing false alarms by clouds.

Due to the similar appearance of smoke and clouds, identification of smoke is better achieved by using *SeaStar*/*SeaWiFS* radiometer, because it has wide spectral coverage comprising the visible (*ch.1*, 0.41 µm, to *ch.6*, 0.67 µm), and near-infrared (*ch.7*, 0.76 µm and *ch.8*, 0.86 µm) wavebands. All channels pertain to certain attributes of fire smoke plume, but contain different information.

SeaWiFS measures light intensity in several bands. The measurements allow quantification of light absorption and subsequent estimation of fires. *SeaWiFS* improves by having better bands for atmospheric correction (*i.e.*, removing the effect of light scattering by the Earth's atmosphere), which will particularly aid the estimation of forest fires smoke.

In light of their unique and important role, *SeaWiFS* smoke detection scenes are the focus of this work. This paper presents an idea which derives from the fusion of the satellite images. The images resulting from only one process are not enough with the thematic requests for the diagnosis and the treatment. However, to separately observe a series of multimode images of a same object is not a better solution. The fusion of these data is thus a paramount stage.There are three methods of fusion:

1. Statistical methods, like *PCA* (Principal Component Analysis) method.

2. Methods resulting from signal processing, like *WT* (Wavelet Transformer) method.

3. Colorimetric methods, like *FAC* (Fusion by Arithmetic Combination) of spectral bands method.

The *FAC* method is classified in the colorimetric part, because it is often used with an aim of visual improvement of the data. Of all the methods used, it is simplest, however, its effectiveness depends on the data input. The images are mixed by addition and/or subtraction and/or product, after D-sampling of the data to the same size. This method is selected in this work.

Each image in this paper is converted from *RGB* (Red, Green and Blue) field to *HSI* (Hue, Saturation and Intensity) field. We seek to obtain the maximum of smoke plumes pixels on the images, then one looks at the values taken by intensity and saturation for potentially applying them to other images in routine.

2. Material

2.1. Sensor description

The *SeaWiFS* instrument on board of the *SeaStar* spacecraft is an eight-band radiometer covering wavelengths between 402–885 nm.

The *SeaWiFS* instrument consists of an optical scanner and an electronics module (line drawing). Table 1 is a listing of the central wavelengths and bandwidths for *SeaWiFS*. Applications for imagery include fishing, agriculture, naval operations, and environmental [14].

T a b l e 1. *SeaWiFS* sensor description.

Instrument Bands	
Band	Wavelength
1	402–422 nm
2	433–453 nm
3	480–500 nm
4	500–520 nm

Table 1. Continued.

5	545–565 nm
6	660–680 nm
7	745–785 nm
8	845–885 nm
Mission characteristic*s*	
Orbit type	Sun synchronous at 705 km
Equator crossing	Noon +20 min, descending
Orbital period	99 minutes
Swath width	2.801 km LAC/HRPT (58.3 degrees)
Swath width	1.502 km GAC (45 degrees)
Spatial resolution	1.1 km LAC, 4.5 km GAC
Real-time data rate	665 kbps
Transmission frequency	1702.5 MHz (encrypted)
Revisit time	1 day
Digitization	10 bits

2.2. SeaWiFS level-1A data

There are Level-1A products for each of the following data types: global-area coverage (*GAC*), local-area coverage (*LAC*), lunar calibration, solar calibration, and High Resolution Picture Transmission (*HRPT*) for direct-readout data [15]. *GAC* data are sub sampled from full-resolution data with every fourth pixel of a scan line (from *LAC* pixels 147 to 1135) and every fourth scan line being recorded for each swath (the Earth data collection portion of an orbit). Thus, *GAC* data are comprised of 2048 pixels per scan line, whereas all other types are comprised of 1285 pixels per scan line. A *GAC* scene will also represent an entire swath; whereas *LAC* scenes are defined by the number of continuously recorded scans, and *HRPT* scenes are defined by the number of continuously received scans from one satellite pass [16].

2.3. Smoke and fires detection

SeaStar/SeaWiFS radiometer, has two major advantages for fires smoke monitoring. First, the instrument provides daily coverage of the entire planet at a moderate spatial resolution (approximately 1 km), which is critical for operational global fire monitoring. Second, it has wide spectral coverage comprising the visible (*ch.1*, 0.41 µm, to *ch.6*, 0.67 µm), and near-infrared (*ch.7*, 0.76 µm and *ch.8*, 0.86 µm) wavebands. All channels pertain to certain attributes of fire smoke plume, but contain different information. Smoke is more discernible in the visible channels, which has been employed to estimate fire smoke and trace gas emissions [17]. However, due to the similar appearance of smoke and clouds in each SeaWiFs visible channel, identification of smoke is better achieved with *RGB* (*R*: Red, *G*: Green, *B*: Blue) and *HSI* (*H*: Hue, S: *S*aturation, *I*: Intensity) combinations of these channels [18].

3. Methods

3.1. RGB to HSI components conversion

The colour of a pixel with coordinates (x, y), denoted as $f(x, y)$, is a triplet (r, g, b), where r, g, and b are the intensities of the R, G, and B components, respectively. The origin $(0, 0)$ is at the upper-left comer of an image with the x-axis horizontal and the y-axis vertical.

The three components of the *HSI* colour model (Fig. 1) are hue (H), saturation (S), and intensity (I, or brightness). Hue represents a dominant (pure) colour as perceived by an observer. Saturation refers to the amount of white light mixed with a hue. Two important facts make the *HSI* colour model useful to simulate the colour sensing properties of the human visual system. First, the intensity component is decoupled from the colour information in an image. Second, the hue and saturation components are intimately related to the way in which human beings perceive colour. The geometric conversion from the familiar *RGB* colour model to the *HSI* colour model can be found in Fig. 1. In the following Eqs. (1)–(4), the formulas for conversion are listed for reference [19].
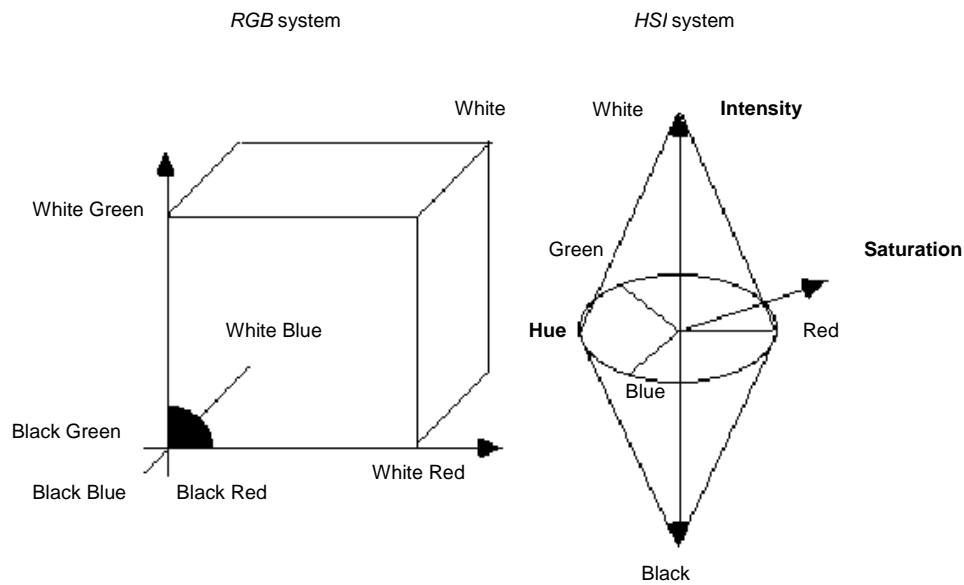
Fig. 1. Geometric representation of RGB and HSI systems.

$$i = \frac{1}{3}(r + g + b) \tag{1}$$

$$s = 1 - \frac{3}{(r + g + b)}\left[\min(r, g, b)\right] \tag{2}$$

$$h = \begin{cases} \theta & \text{if } b \le g \\ 360 - \theta & \text{if } b > g \end{cases} \tag{3}$$

where

$$\theta = \sec\left\{ \frac{\frac{1}{2}[(r-g)+(r-b)]}{\left[(r-g)^2 + (r-b)(g-b)\right]^{1/2}} \right\} \tag{4}$$

3.2. Building a smoke plume feature model

In the study of image-based smoke detection, it is necessary to build a more precise smoke plumes feature model for vision-based smoke plumes detection systems. In this research, we used two *SeaStar/SeaWiFS* images carrying various dates and areas to analyze the colour features of smoke plumes according to the *HSI* colour model.

A colour set, *C*, is a set of colours such that for each colour in the set, represented as a triplet (h, s, i) in the *HSI* colour model, the following conditions are satisfied: $[h_{min} \le h \le h_{max}]$, $[s_{min} \le s \le s_{max}]$, and, $[i_{min} \le i \le i_{max}]$ in which $[h_{min}, h_{max}]$ is the range of hue, $[s_{min}, s_{max}]$ is the range of saturation, and $[i_{min}, i_{max}]$ is the range of intensity of the colour set *C*. Formally, the colour set may be denoted as:

$$C(h,s,i) = \left\{ (h,s,i) \middle| h_{min} \le h \le h_{max}, s_{min} \le s \le s_{max}, i_{min} \le i \le i_{max} \right\} \tag{5}$$

The colour separation algorithm for an input image $f(x, y)$ based on some smoke plumes colour set *C* is as follows: or each pixel in the image, if the colour of the pixel does belong to the colour set, then set the pixel colour to red; otherwise, keep the pixel colour unchanged (a background colour, unchanged). The result image $g(x, y)$ after performing the above colour separation can be represented as:

$$g(x, y) = \begin{cases} \text{red,} & \text{if } f(x, y) \in C \\ f(x, y), & \text{otherwise} \end{cases} \tag{6}$$

4. Results and discussions

In our case, we have used Local Area Coverage Level *1A* images with spatial resolution of 1.1 km at nadir. This class of filenames begins with the following convention: *syyyydddhhmmss*, where *s* denotes the sensor (currently *S* for *SeaWiFS*, *A* for *Aqua-MODIS*, and *T* for *Terra-MODIS*), *yyyy* is the year, *ddd* is the day of the year (001–366), *hh* is the hour (*UTC*) when the sensor began collecting the scene's data (00–23), *mm* is the minute (00–59), and *ss* is the second (00–59).

Each image product in this paper is generated from a corresponding Level-1A product. The main data contents of the product are the geophysical values for each pixel, derived from the Level-1A raw radiance counts by applying the sensor calibration, and atmospheric corrections.

The radiometric operation of calibration is used to eliminate the side effects on the rough images. They are corrections of the true brightness measured by the radiometer SeaWIFs in order to eliminate the effects of the atmosphere and the solar angle of illumination. Therefore, the effect of incoming solar radiation on the model colorimetric is compensated.

a

b
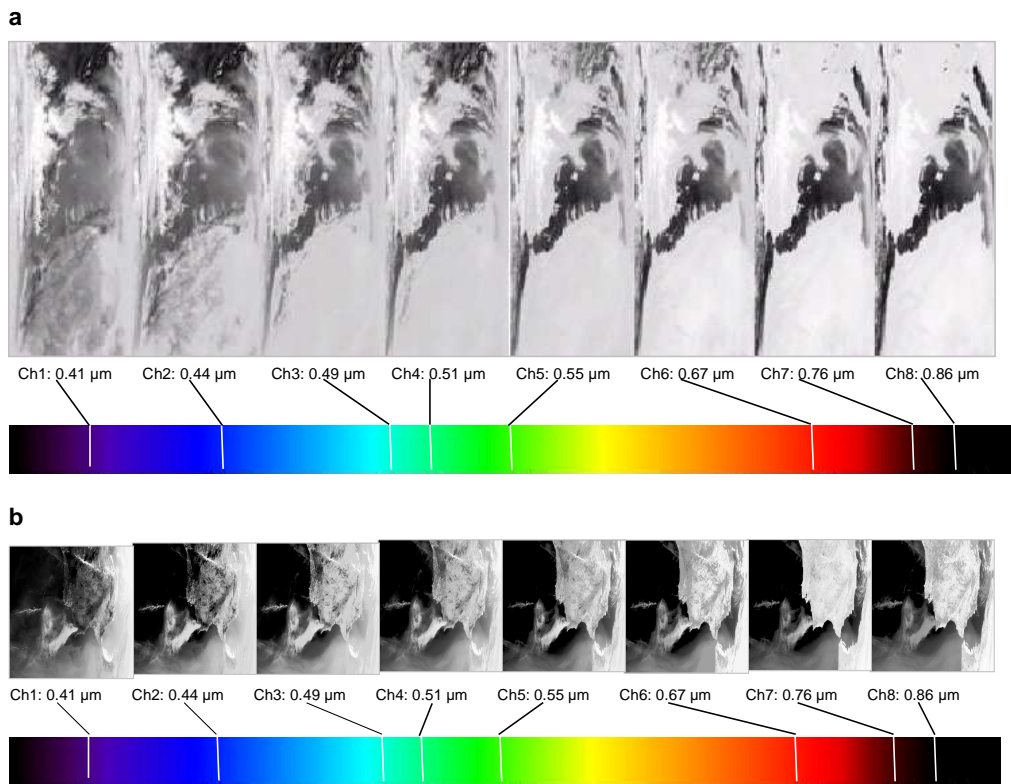
Fig. 2. Eight spectral channels of *image A* (reference image) with the representation of the central spectral wave of each band (**a**), eight spectral channels of *image B* with the representation of the central spectral wave of each band (**b**).

Figure 2**a** shows the eight raw channels (6 visible and 2 *NIR*) of image *A* (labelled in this work); all channels are splitted and radiometrically calibrated by using *ENVI* Software (the Environment for Visualizing Images, Research Systems, Inc., Boulder, *USA*). The file of this image named *S2000238120538.L1A_MLAC* was received from official source (*OCEANCOLOUR GSFC NASA US* data base). In this case, our image was received on day 238 (25 August) of year 2000 at 12:05:38 *UTC*.

For each band, the detector measures the intensity of the light that reaches the sensor. When these data are displayed visually, the result is a series of gray-scale images. Notice how different features have different intensities in the various bands. For example, clouds and water appear bright in the blue and purple bands, while land is dark. In the red and infrared bands, it is the land that is bright, while the water is dark.

Image A is used to process forest fires smoke pixels covering the North African Coast. Because of the important number of forest fires smoke pixels on this image, it is considered like the reference image in this work.
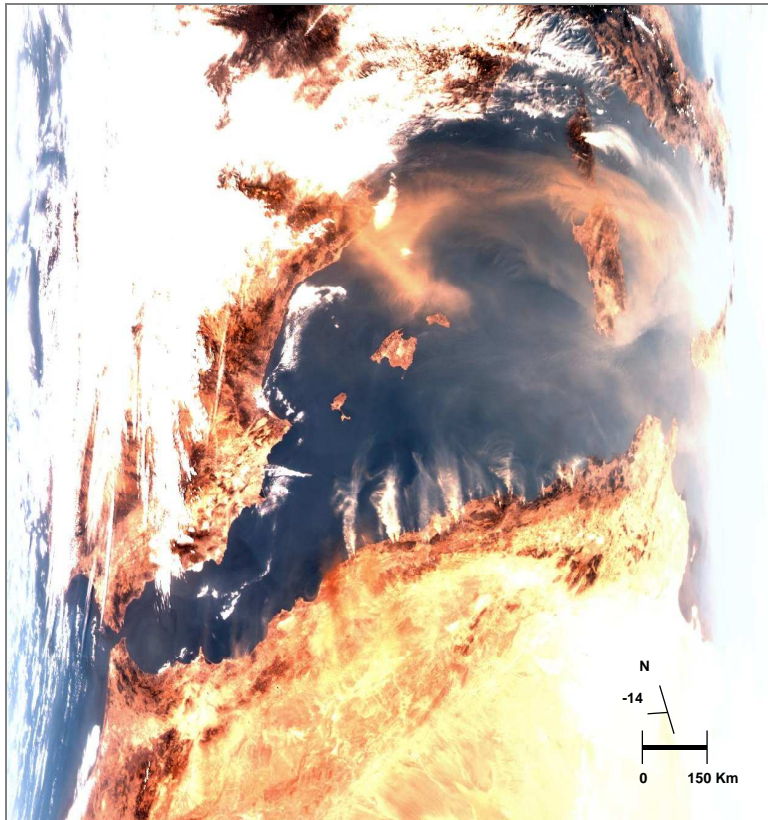
Fig. 3. *R*: *ch3*, *G*: *ch2*, *B*: *ch1* combination result.

By *RGB* combination between visible channels 3, 2 and 1 successively (*R*: *ch3*, *G*: *ch2*, *B*: *ch1*) from image *A*, we can watch clearly the smoke from fires along the North African coast Fig. 3. This combination most closely represents fires smoke in the visible spectrum. Winds generated large quantities of smoke dust storms, which blanketed the Mediterranean Sea. This event can be also clearly watched on the high right part from image of Fig. 4. This image was realised by combination between the

visible and the *NIR* channels. We have used the following combination *R*: *ch7*, *G*: *ch4*, *B*: *ch1*.
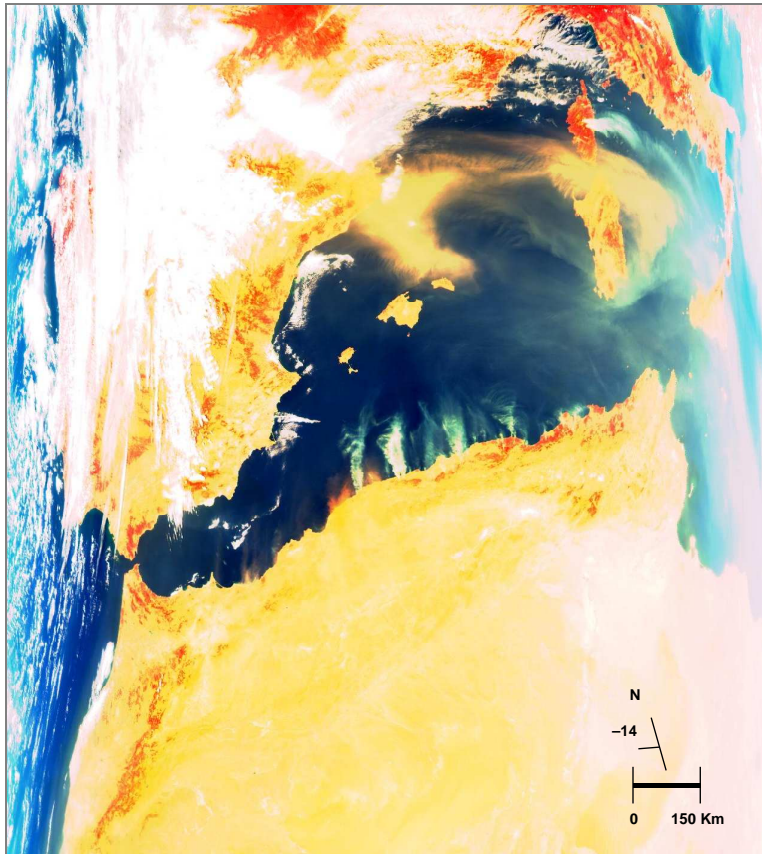
Fig. 4. *R*: *ch7*, *G*: *ch4*, *B*: *ch1* combination result.

The colour separation algorithm is applied to channel 1, 2 and 3 from image *A*, by using *r*: *ch3*, *g*: *ch2*, *b*: *ch1* combination in Eq. (1). The result image is given in Fig. 5. In this image, we can watch the intensity edges of smoke plumes presented as red colour separation.

Saturation pixels are calculated by using the same combination (*i.e. r*: *ch3*, *g*: *ch2*, *b*: *ch1* combination) in Eq. (2), the result is given in Fig. 6. In this image, the region of interest was selected, and the red mask of separation presents the areas of smoke plumes.

The other event, on 13 September 2003 – a huge plume of smoke drifts westward over the Atlantic Ocean from a massive forest fire in South-Western Portugal. This event (image *B* of Fig. 2**b**) is acquired by Sea-viewing Wide-Field-of View Sensor (*SeaWiFS*) from the *SeaStar* satellite.
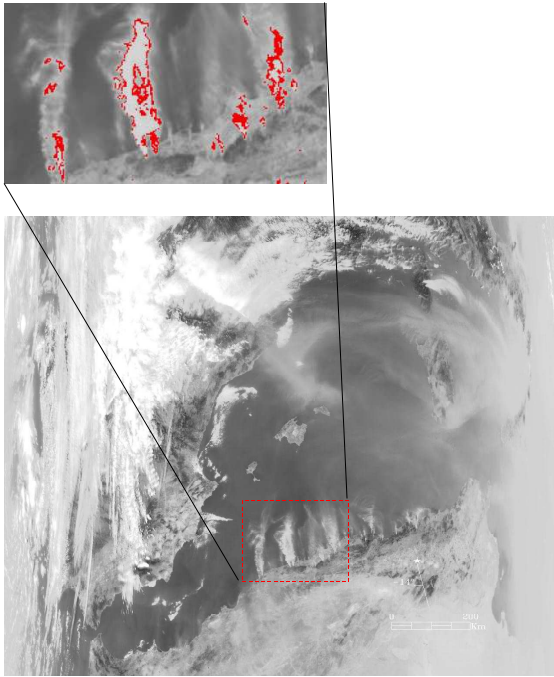
Fig. 5. Extraction of the edge of fires smoke pixels from the intensity image (image *A*).
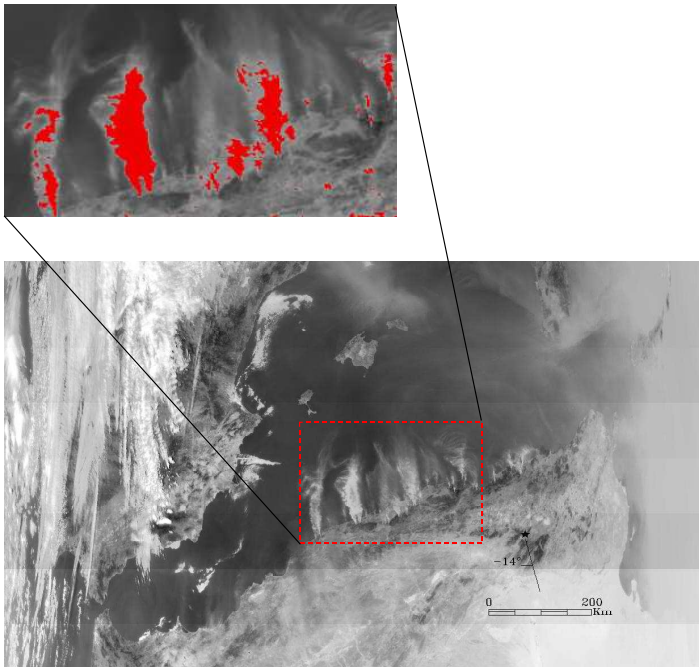
Fig. 6. Extraction of maximum fires smokes pixels from saturation image (image *A*).

Figure 2**b** shows the eight spectral channels of the image *B* (all channels are radiometrically calibrated), whose file is named *S2003256132227. L1A_MLAC* was acquired on 13 September 2003 and covers the forest fires smoke pixels in the south west of Portugal. This image is used to validate our research.

The HIS color model has been adopted because it is intimately related to the way in which human beings perceive colors. According to the empirical analysis of the set of forest fires images, the hue values for forest fires flames from red to yellow are usually in the range of [0°–60°]. The range of [200°–280°] includes the higher temperature flames. This point is not discussed in our research.

The intensity values in image *A* are in the range [230, 980] and, on the other hand, the intensity values in image *B* are in the range [184, 1023]. The saturation values after normalization are distributed in the range [0, 100] in the two images. By using colour separation algorithm (Eq. (6)) in image *A*, the saturation values from the smoke pixels are in the range [65, 80], and the intensity values from the smoke pixels are in the range [780, 800].
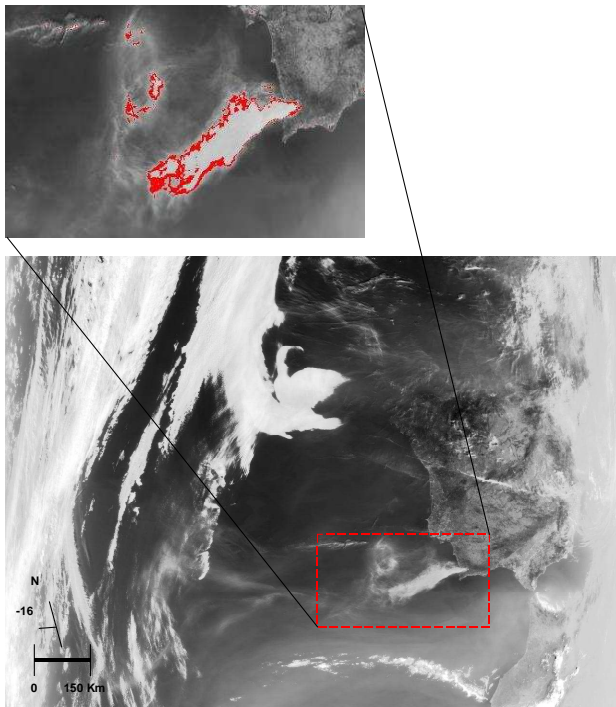
Fig. 7. Extractions of the edge of fires smoke pixels from the intensity image (image *B*).

By using the same *RVB* combination and the same intervals of the smoke plumes extracted from image *A* and Eq. (1), Eq. (2) and Eq. (6) (Saturation: [780–800], Intensity: [65–80], Hue: [0°–60°]), the active forest fires smoke locations in image *B* have been enhanced and edged in red colour. In Fig. 7 and Fig. 8, we can watch respec-

tively, the intensity edges and saturation pixels of smoke plumes presented as red col-
our separation. The limit values for the fires smoke with *HSI* system are summarized
in Table 2 for each image.

Table 2. List of images used.

Environment	Date of acquisition	Start time of acquisition (*UTC*)	Region
Image A (image reference)	25 August 2000	12 h 05 min 38 sec	North of Algeria
Image B	13 September 2003	13 h 22 min 27 sec	South West of Portugal
Image C	24 March 2003	06 h 12 min 10 sec	South of the United States of America
Image D	20 December 2002	11 h 50 min 15 sec	West of Africa
Image E	23 January 2003	18 h 21 min 09 sec	South East of Australia
Image F	05 January 2005	08 h 33 min 45 sec	Dominican Republic and Haiti
Image G	20 May 2001	10 h 20 min 55 sec	Angola and Democratic Republic of the Congo
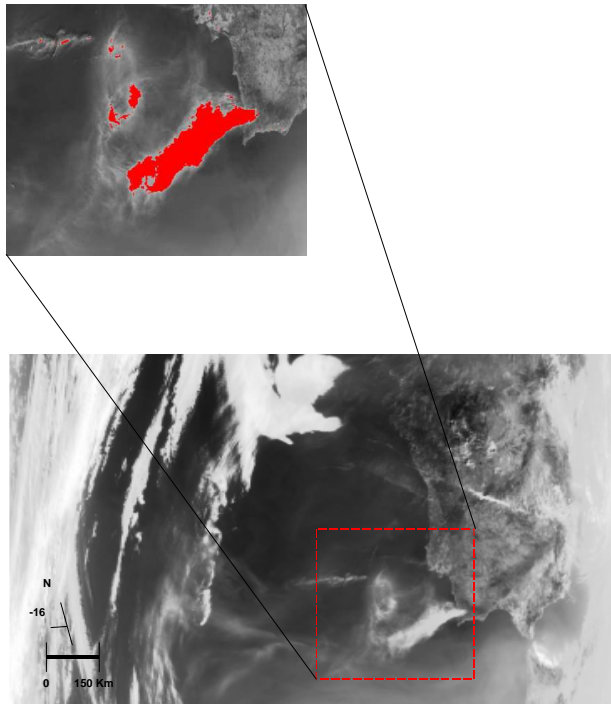
Fig. 8. Extraction of maximum fires smokes pixels from saturation image (image *B*).

For each image (image *A* and image *B*), we used *2-D* scatter plots to present fires
smoke pixels distribution for each image combination selected (visible channels:
channel 2 with channel 3, *IR* channels: channel 7 with channel 8), to compare the fires

smoke pixels in two selected bands as both a scatter plot and in terms of their spatial distribution in each image. Blue pixels show the distribution of fires smoke pixels (Fig. 9**a**–9**d**).

We can observe that fires smoke pixels distribution in both Fig. 9**a** and Fig. 9**c** (visible channels combination) presents a larger part compared to Fig. 9**b** and Fig. 9**d** (*IR* channels combination), which follows from the fact that smoke from forest fires is more discernible in the visible channels.

a

b

c

d
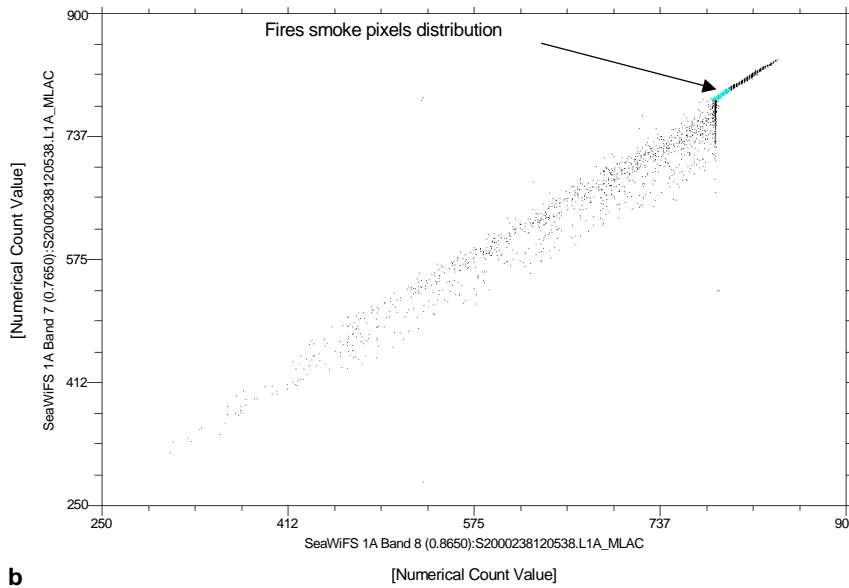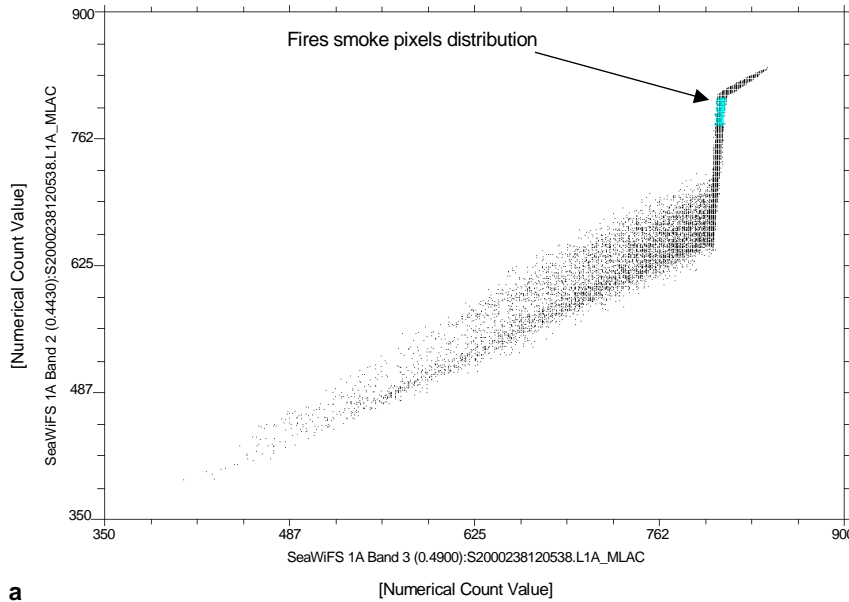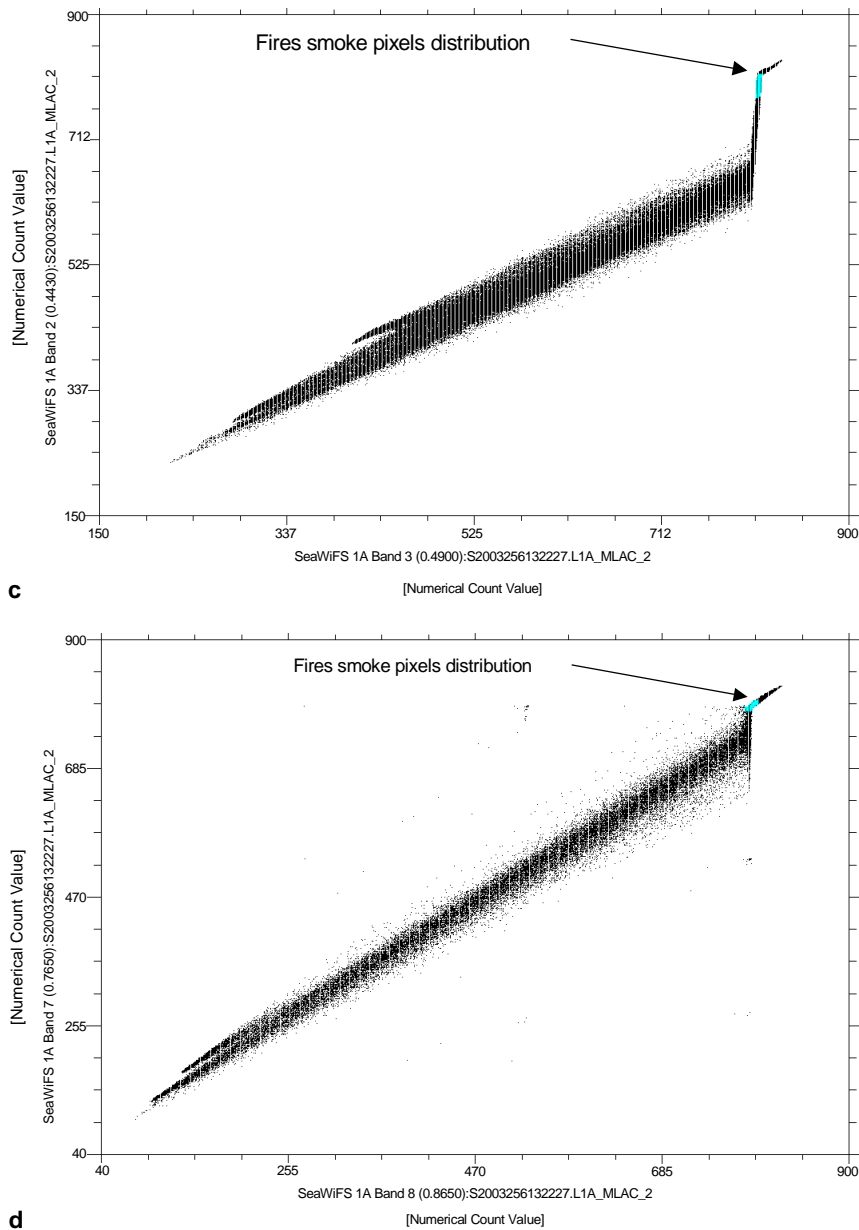
Fig. 9. *2D* scatter plots with fires smoke pixels distribution: image *A*, *ch7*, and *ch3* (**a**), image *A*, *ch7* and *ch8* (**b**), image *B*, *ch2* and *ch3* (**c**), image *B*, *ch7* and *ch8* (**d**).

The proposed forest fires smoke method is tested with five other scenes of images (image *C* to image *G* in Table 2) for a variety of conditions, including different regions of the planet and different times. The experimental results of the proposed method are shown in Table 3.

Table 3. Features of fires smoke.

Environment	Hue [°]	Saturation (S)	Intensity (I)
Image A (reference)	0–60	0–100	230–980
Smoke plume coverage A		65–80	780–800
SPRR [%]		0	0
Image B	0–60	0–100	180–1023
Smoke plume coverage B		66–81	782–800
SPRR [%]		0.342	0.0633
Image C	0–60	0–100	130–986
Smoke plume coverage C		65–79	780–801
SPRR [%]		0.346	0.0316
Image D	0–60	0–100	240–980
Smoke plume coverage D		65–82	779–802
SPRR [%]		0.685	0.0949
Image E	0–60	0–100	156–898
Smoke plume coverage E		66–81	780–800
SPRR [%]		0.342	0.0
Image F	0–60	0–100	80–1020
Smoke plume coverage F		64–80	781–798
SPRR [%]		0.346	0.0950
Image G	0–60	0–100	250–988
Smoke plume coverage G		67–79	778–799
SPRR [%]		1.031	0.0950

Smoke Pixel Reference Ratio *SPRR* denotes the detection rate between each image from Table 2 and the reference image (image *A*). It is defined as the ratio

$$SPRRi[\%] = \frac{\left|Vi\max - Vif\max\right| + \left|Vi\min - Vif\min\right|}{Vi\max + Vif\max + Vi\min + Vif\min} \cdot 100 \tag{7}$$

for the Intensity images and

$$SPRRs[\%] = \frac{\left|Vs\max - Vsf\max\right| + \left|Vs\min - Vsf\min\right|}{Vs\max + Vsf\max + Vs\min + Vsf\min} \cdot 100 \tag{8}$$

for the saturation images. In the above equations *Vimax* and *Vsmax* indicate respectively the maximum value of the intensity and the saturation in each image (from image *A* to image *G*), while *Vimin* and *Vsmin* are respectively the minimum value of the intensity and the saturation in each image (from image *A* to image *G*). On the other hand, *Vifmax* and *Vsfmax* are respectively the maximum value of the intensity and the saturation of forest fire smoke pixels in each image (from image *A* to image *G*), *Vifmin* and *Vsfmin* are respectively the minimum value of the intensity and the saturation of forest fire smoke pixels in each image (from image *A* to image *G*). The *SPRR* ratio is applied

to establish the efficiency of our method to localise the forest fires smoke pixels for various environments.

We can observe in Table 3 that the values of the *SPRRs* [%] and the *SPRRi* [%] are respectively in the interval [0.342, 1.031] and [0.0316, 0.0950]. In general, these results are very encouraging and promising, because the method can detect maximum pixels of smoke plumes. The largest values are observed in image *G*, because of a small area of smoke plumes in this scene of image (Fig. 10).
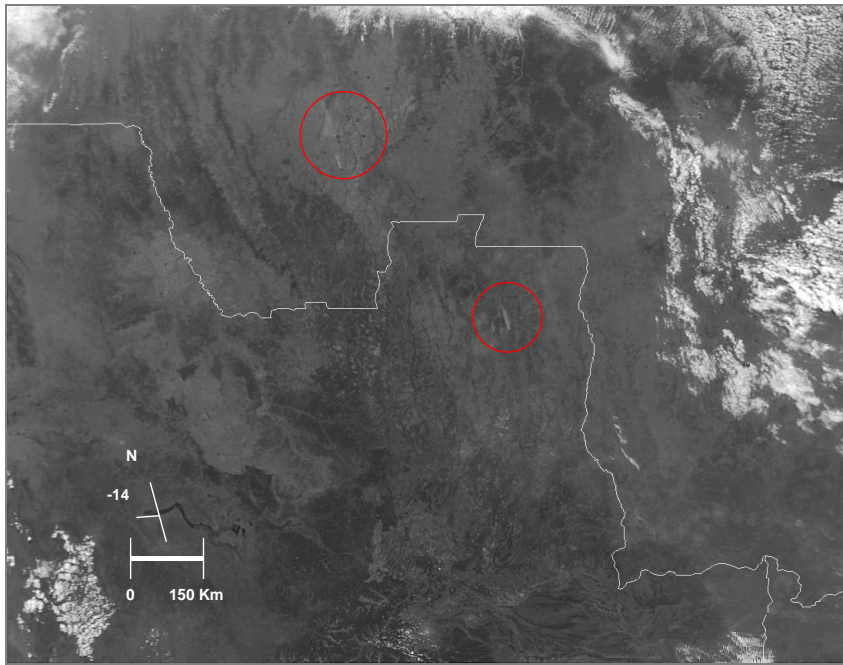
Fig. 10. Image *G*: Angola and Democratic Republic of the Congo region with a small area of smoke plumes.

5. Conclusions

This paper presents an overview of one of the environmental phenomena: forest fires smoke. The *RGB* combination method (colorimetric method) is the aim of our present work to extract the smoke pixels. This purpose will be designed primarily for use with *SeaWiFS* data, because of the long field of view in the visible spectrum of the onboard sensor. Each band is displayed in a monochromatic scale corresponding to its appropriate color. When these are mixed, they produce the entire range of visible colors, creating an image that is fairly close to what the human eye would perceive.

A new method derived from the *RGB* combination based on the computer vision techniques and some theory of chromatics is proposed. The colour masking technique is proposed to extract the maximum fires smoke pixels from the *SeaStar/SeaWiFS*

images. As a result, smoke plumes pixels are obtained visually on the images intensity and saturation; then one looks at the values taken by intensity and saturation for potentially applying them to other images in routine.

We validated the proposed method by using other scenes of images with different dates and different regions (seven images). The obtained results show that the method can detect maximum pixels of smoke plumes. We found the results almost identical to treat forest fires smoke pixels.

Some limitations of the method proposed are represented as follows:

– this method is used only in diurnal period of day,

– smoke generated by the higher temperature flames; this point is not discussed in the present work,

– in a few cases, this method couldn't distinguish clouds and dust storms from fires smoke pixels,

– small areas of smoke plumes cannot be depicted by the proposed method in some cases.

References

[1] CRUTZEN P.J., HEIDT L.E., KRASNEC J.P., POLLOCK W.H., SEILER W., *Biomass burning as a source of atmospheric gases, CO, H2O, N2O, NO, CH3CL and COS*, Nature **282**(5736), 1979, pp. 253–256.

[2] CRUTZEN P.J., ANDREAE M.O., *Biomass burning in the tropics: Impact on atmospheric chemistry and biogeochemical cycle*, Science **250**(4988), 1990, pp. 1669–78.

[3] KAUFMAN Y.J., JUSTICE C., FLYNN C.L., KENDALL J., SETZER A., *Potential global fire monitoring from EOS-MODIS*, Journal of Geophysical Research **103**, 1998, pp. 32215–38.

[4] KAUFMAN Y.J., FRASER R.S., *The effect of smoke particles on clouds and climate forcing*, Science **277**(5332), 1997, pp. 1636–39.

[5] REID J.S., HOBBS P.V., RANGNO A.L., HEGG D.A., *Relationships between cloud droplet effective radius, liquid water content, and droplet concentration for warm clouds in Brazil embedded in biomass smoke*, Journal of Geophysical Research **104**(D6), 1999, pp. 6145–53.

[6] LI Z., BARKER H., MOREAU L., *The variable effect of clouds on atmospheric absorption of solar radiation*, Nature **376**(6540), 1995, pp. 486–490.

[7] LI Z., *Influence of absorbing aerosols on the solar surface radiation budget*, Journal of Climate **11**, 1998, pp. 5–17.

[8] SIFAKIS N., PARONIS D., KERAMITSOGLOU I., *Combining AVHRR imagery with CORINE Land Cover data to observe forest fires and to assess their consequences*, International Journal of Applied Earth Observation and Geoinformation **5**(4), 2004, pp. 263–74.

[9] JUSTICE C.O., MALINGREAU J.P., SETZER A.W., *Satellite remote sensing of fires: Potentials and limitations*, [in:] *Fire in the Environment*, [Eds.] P.J. Crutzen, J.G. Goldammer, John Wiley and Sons Ltd., 1993, p. 77–88.

[10] SETZER A.W., MALINGREAU J.P., *AVHRR monitoring of vegetation fires in the tropics: Toward the development of a global product*, [in:] *Biomass Burning and Global Change*, ed. J.S. Levine, The MIT Press, Cambridge, 1996, pp. 25–39.

[11] RAJEEV K.J., SAUMITRA M., KUMARAN D.R., RAJESH S., *Forest fire risk zone mapping from satellite imagery and GIS*, International Journal of Applied Earth Observation and Geoinformation **4**(1), 2002, 1–10.

[12] KIBLER J., *The Recent and Future Changes of the Hazard Mapping System (HMS) – A Multiplatform Remote Sensing Approach to Fire and Smoke Detection*, Atmospheric Sciences and Air Quality Conference ASAQC '05, Proceedings, 2, 2005, pp. 121–35.

[13] GIGLIO L., DESCLOITRES J., JUSTICE C.O., KAUFMAN Y., *An enhanced contextual fire detection algorithm for MODIS*, Remote Sensing of Environment, 87, 2003, pp. 273–82.

[14] GRÉGOIRE J.M., CAHOON D., STROPPIANA D., *Fundamentals of Remote Sensing*, Canada Centre for Remote Sensing, Quebec 2002, pp. 68–69.

[15] LEBLON B., GARCÍA P.A.F., OLDFORD S., MACLEAN D.A., FLANNIGAN M., *Using cumulative NOAA-AVHRR spectral indices for estimating fire danger codes in northern boreal forests*, International Journal of Applied Earth Observation and Geoinformation, **9**(3), 2007, 335–42.

[16] HASSINI A., BENABADJI N., BELBACHIR A.H., *Reception of the APT Weather Satellite Images*, Association for the Advancement of Modelling and Simulation Techniques in Enterprises (AMSE) Journal, Advances B, France, **48**(1), 2005, pp. 25–43.

[17] KAUFMAN Y.J., REMER L.A., *Detection of forests using mid-IR reflectance: An application for aerosol studies*, IEEE Transactions on Geoscience and Remote Sensing, **32**, 1994, pp. 672–83.

[18] HASSINI A., BENABADJI N., HASSINI N., BELBACHIR A.H., *Forest Fires Smoke Detection from SeaWiFS Sensor Data: Case of Algerian Coast*, International, Conference on Information and Communication Technologies: From Theory to Applications, IEEE Proceedings, 1, 2006, pp. 412–17.

[19] HOMG W.B., PENG J.W., CHEN C.Y., *A New Image-Based Real-Time Flame Detection Method Using Color Analysis*, IEEE Networking, Sensing and Control Proceedings, 2005, pp. 100–05.